Article

In Operando *μ*CT Imaging of Silylated Silica Aerogels during Ambient Pressure Drying and Spring-Back

Published as part of the Chemistry of Materials virtual special issue "In Honor of Prof. Clement Sanchez".

Julien Gonthier,* Tilman Rilling, Ernesto Scoppola, Fabian Zemke, Aleksander Gurlo, Peter Fratzl,* and Wolfgang Wagermaier*

Read Online

ACCESS | Metrics & More | Article Recommendations | SI Supporting Information

ABSTRACT: Aerogels are solid materials with a porous structure filled with air and are among the best thermal insulation materials. During ambient pressure drying (APD), silica gels endure significant drying shrinkage due to the capillary pressure generated by pore liquid evaporation. Silylated gels can recover the drying shrinkage through a phenomenon called the spring-back effect (SBE). However, the underlying structural mechanisms and the evolution of the amount of liquid and gaseous phases in the pores of a gel undergoing APD remain unexplored. Here, we use in operando X-ray micro-computed tomography (*μ*CT) with quantitative imaging to monitor the progression of the liquid, gaseous, and solid phases of silica gels during APD, i.e., during the drying shrinkage and the subsequent SBE. Silica gels modified by trimethylchlorosilane shrank to 17% of their original volume and sprung back to 29% of their original volume. We found that a mixture of gaseous and liquid phases is already present in gels before the maximum shrinkage, which challenges the common assumption that gas penetrates the pores in parallel to the SBE. The emergence of the SBE was correlated to an equal volume fraction of solid, liquid, and gas in the gels. The evaporation rate decreased near and after the maximum shrinkage, suggesting a shift from convection-limited to diffusion-limited transport of hexane vapor. Our results show that fluid movements and volume change can be monitored in operando by *μ*CT imaging during ambient pressure drying and spring-back of an aerogel, showing the combined effects of evaporation of fluid and diffusion of gas within and out of the aerogel.
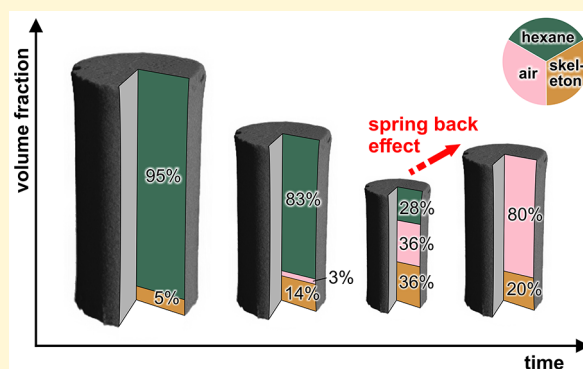
INTRODUCTION

Aerogels are porous solid materials whose pores are filled with air or vacuum. They have an open porous network that makes up for more than 90% of their volume and show a very high specific surface area.[1,2] Several functional properties emerge from the aerogel's unique structure, such as extremely low thermal conductivity, compressibility, and catalytic activity, and they can be exploited as a reusable sorbent to clean-up organic liquids.[3−7] Silica aerogels are among the most cost-effective to produce, and their syntheses and properties are well documented.[8] There is a growing interest toward the industrial implementation of silica aerogel-based thermal insulators due to their high insulation performances and optical properties, notably allowing aesthetic incorporation in buildings.[9−11]

Silica aerogels are commonly produced via a sol−gel process. A suspension of nanoparticles is formed from a silicon alkoxide or sodium silicate precursor (sol), and the particles are cross-linked to create a continuous solid network with liquid filled pores (gel, or alcogel if the liquid is an alcohol). An aerogel is obtained by exchanging the pore liquid of a gel for air without significant volume shrinkage and alteration of the solid network. Supercritical drying is an efficient drying method but remains technically challenging, expensive, and time-consuming, making ambient pressure drying (APD) potentially better suited for industrial production.[1,12] During APD, the small size of the pores creates strong capillary forces upon evaporation of the pore liquid. The tension in the liquid is balanced by a compression of the solid network, resulting in a significant shrinkage of the gel volume. In untreated gels, drying shrinkage brings the particles of the solid network closer together, promoting condensation reactions between surface silanol groups. These reactions
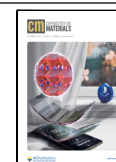
lock the solid network and lead to irreversible shrinkage, resulting in a dense dry gel called xerogel.[2] This can be prevented by modifying the surface chemistry of the particles prior to APD using silylating agents that react with surface silanol groups. The surface modification alleviates condensation reactions by introducing functional groups, making drying shrinkage reversible. Several silylating agents are reported in the literature, such as trimethylchlorosilane (TMCS).[13−18] This reversible shrinkage in modified gels is known as the spring-back effect (SBE).

The extent of the SBE dictates the final properties of monolithic aerogels prepared by APD and is an indicator of the quality of the dry gel. Different quantities are used in the literature, some authors report the "volume shrinkage" defined as $1 - V^d/V^0$, with V^d and V^0 as the dry and initial volume of the gel, respectively.[14,19−21] Hwang et al. refer to the "spring-back efficiency" as V^d/V^0, where V^0 is the volume of the alcogel before modification.[16,17] Sivaraman et al. define the "APD shrinkage" as an approximation of the volume shrinkage by ρ_{APD}/ρ_{SCD}, where ρ is the bulk density of gels dried by APD or SCD, respectively.[22] In this paper, the authors adopt a similar definition of the spring-back efficiency introduced by Hwang et al. based on the volume of the alcogel before drying. The spring-back efficiency varies considerably depending on the material and drying process, and it can range from 30 to almost 100 vol % for silylated silica gels (see precedent references). This relates to a significant deformation of the solid network, considering that during APD, a gel may reach a maximum shrinkage of about 20 vol % of its original volume.[16,23,24] Silylated silica gels can thus endure and recover the drying shrinkage during APD without macroscopic failure, showing a remarkable deformability for a ceramic-based material, which is not observed in other forms of silica like glass or quartz.

Despite being a well-known phenomenon in the production of aerogels by APD, little is known about the physical mechanisms and related material structure evolution at the nanoscale behind the spring-back effect. Only few studies have tackled the conditions of its emergence and result in structural and compositional changes, while the impact of the synthesis, aging, surface modification, and drying on the spring-back efficiency has been exhaustively studied.[8,15,17,20,25−28] The reversible shrinkage inherent to the SBE in silylated silica aerogels unveils fundamental research questions on the deformability of porous ceramic materials, and a better understanding of the SBE may give insights for improving the production of aerogels by APD. However, it is difficult to quantitatively track structural and compositional variations during drying as it generally requires a controlled environment under ambient conditions and the use of non-destructive methods. To this regard, small-angle X-ray scattering (SAXS) and X-ray micro-computed tomography (μCT) methods are well suited and provide enough space for experiments on gels contained in a drying chamber. Zemke et al. notably used synchrotron-based SAXS and monitored the drying of silica aerogels enclosed in a custom chamber under ambient pressure conditions.[24] While SAXS provides structural information from 2 to 500 nm,[29] μCT can generate 3D volumes of samples of various sizes with a maximum resolution of about 1 μm while also providing the reconstructed attenuation coefficient (RAC) values of a sample.[30,31] This distinct advantage over SAXS potentially permits to extract quantitative compositional information of hybrid materials such as aerogels but does not allow us to resolve aerogels structural heterogeneities,

which extend to about 100 nm.[32] μCT was not explored as a method to characterize monolithic aerogels besides a few studies.[18,33,34]

In this paper, we report the geometric changes of TMCS-modified and unmodified silica gels during APD by an in operando μCT method and we propose a procedure based on μCT quantitative imaging to calculate the evolution of the total volume of silica skeleton, pore liquid, and gas in the drying gels. The drying shrinkage and SBE are correlated to the porosity and composition of the pores during drying. The skeletal density calculated by μCT quantitative imaging is compared to typical values determined by helium pycnometry, and the reliability of the method is discussed. The data on the xerogels resulting from the drying of unmodified gels are challenged by simulating condensation reactions related to drying shrinkage. We show that gas and liquid are simultaneously present in the gel before the SBE.

■ EXPERIMENTAL SECTION

Synthesis. Silica alcogels were produced by a two-step sol−gel synthesis adapted from refs 14 and 18. A silica sol (53 mL) was prepared by mixing 14.58 g (0.07 mol) of tetraethyl orthosilicate (98%, Sigma-Aldrich) with 6.130 mL of ethanol (99.96%, VWR Chemicals), 6.130 mL of a solution of hydrochloric acid (37%, Carl Roth) in ethanol (2.449×10^{-4} vol %), and 1.260 mL of water. The sol was covered and stirred for 90 min. Ethanol (16.13 g) was added, and 3.285 mL of a solution of ammonium hydroxide (25%, Merck) in water (6.678×10^{-3} vol %) was introduced dropwise to promote the gelation. The sol was covered and stirred slowly for 30 min and was then casted into two-part molds made of polyether ether ketone (PEEK) using a micropipette. The molds have eight cylindrical slots with a depth and diameter of 16 and 8 mm, respectively (Figure S1a), and each slot was filled with 785 μL of solution, resulting in cylindrical samples each containing 1.04×10^{-3} mol of SiO_2. After casting, the sol was defoamed at room temperature by applying a light vacuum for 2 min in a desiccator to remove the air dissolved in the sol. Each mold was inserted in a closed polytetrafluoroethylene (PTFE) container and left to gel at 50 °C for 24 h. Upon unmolding, the silica gels were splashed with ethanol to prevent drying and were stored in 1.2 L of ethanol per mole of SiO_2 at room temperature for 24 h. Ethanol was exchanged for n-hexane (99%, Carl Roth) stepwise by replacing the initial volume of ethanol for an equivalent volume of mixtures of 25/75, 50/50, and 75/25 vol % of n-hexane in ethanol every 24 h. The gels were rinsed four times with the same volume of n-hexane every 24 h. Some gels were then modified with trimethylsilyl chloride (TMCS; 99%, Sigma-Aldrich). The surface modification was conducted in four steps successively replacing n-hexane by the same volume of a TMCS in n-hexane solutions of 3, 3, 6, and 6 vol % every 24 h. The total TMCS/SiO_2 molar ratio was 1.7. The modified gels were finally rinsed with the same volume of n-hexane every 24 h four times and were stored in n-hexane. The samples were stored for different durations before drying, up to 6 months.

In Operando APD by μCT. Five modified and two unmodified silica gels were dried at ambient pressure using an in operando μCT method for a total of seven samples. The modified gels are labeled M1−M5 and the unmodified gels U1−U2. Prior to μCT experiments, a sample was transferred from its n-hexane storage solution into a tailored PEEK chamber closed with a lid (Figure S1b). The chamber was inserted in an EasyTom 160/150 CT system (RX Solutions, Chavanod, France) equipped with a micro-focus tube (tungsten filament) and a flat panel detector (cesium iodide scintillator). The PEEK chamber has a 0.4 mm wall thickness to limit X-ray absorption. The distance between the chamber and the tube was minimized to reach a voxel size of 11 μm while keeping the sample in the field of view during drying. During the APD of a single sample, a series of 141 μCT scans were acquired at a voltage and current of 135 kV and 200 μA, respectively. One scan consisted of 64 projections captured in the step and shot mode without reference images in only 1 min. Each scan

was preceded by a black and gain calibration of 1 and 3 min, respectively. The time step between each tomography was about 6 min, and the total duration of the experiment was ca. 14 h. The first scan was done with the chamber closed, and then, the lid of the chamber was exchanged for a second lid with a 6 mm diameter opening to begin the drying. The moment of the lid exchange was defined as $t = t_0$. The timestamp of each scan was defined as the difference between the average time of the 64 projections and t_0. The reconstruction was performed with a cone beam algorithm in the software XAct (RX Solutions). Back-projection parameters of the first scan were adjusted manually and were used as a template for the 140 remaining scans from the same specimen. Each reconstruction generated a vertical stack of about 1,000 slices in the 8-bit tiff format along the vertical axis of the cylinder. The slices were segmented in the software Dragonfly[35] using an in-house written python script. The segmentation procedure is described in SI1 and generated the following outputs: the volume of the gel: $\tilde{V}_k$, the cross-sectional area of the gel along the z axis of the cylinder: $A_{i,\,k}$, and the gray value averaged over that area: $\tilde{g}_{i,\,k}$, with $i, k \in \mathbb{N}$. i is the vertical voxel coordinate (or the slice number), and k is the scan number. At each scan number corresponds a timestamp t_k. The volume of the gel was corrected, as described in SI2 resulting in V_k. We then defined the spring-back efficiency as the ratio between final volume $V^d = V_{k\,=\,140}$ and initial volume $V^0 = V_{k\,=\,0}$ of the gel. The maximum shrinkage was defined as V^{min}/V^0, with V^{min} as the minimum volume of the gel. To evaluate the accuracy of the automated segmentation procedure, a manual segmentation was performed on 11 randomly selected tomographies among the seven gels at different drying times. The results are presented in SI2. After a few more days of drying, the gels were weighed on a PCE-AB 100 (PCE Deutschland GmbH, Meschede, Germany), and the apparent density was calculated as $\rho_a = m^d/V^d$ with m^d as the mass of the dry gel. Fourier transform infrared (FTIR) spectra were recorded on an IRAffinity-1S spectrometer (Shimadzu Corp., Kyoto, Japan) to confirm the surface modification of the aerogels. One modified and one unmodified gel were ground into a fine powder and were analyzed in the attenuated total reflection mode (ATR). In addition to the scans on the silica gels, two additional measurements were carried out on pure n-hexane and deionized water with the same parameters as for the silica gels. A total of 141 μCT scans were recorded on n-hexane and 16 scans on deionized water.

The drying of TMCS-modified and unmodified gels resulted in monolithic aerogels and monolithic xerogels, respectively (Figure 1).
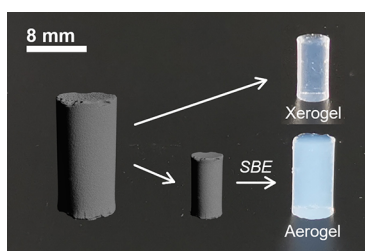

Figure 1. 3D rendering of a gel's volume generated by the automated segmentation procedure at the beginning of drying (left) and at the maximum shrinkage (middle). Visualization done in Dragonfly software. Digital photographs of a xerogel and an aerogel after drying (right).

Some gels had sub-millimeter gas bubbles trapped in them, which presumably came from a mismatch between the two parts of some molds during the gelling of the gels at 50 °C, allowing some air to enter the sol without consequences on the overall μCT analysis. The aerogels show a bluish taint under a black background characteristic of Rayleigh scattering as some air-filled pores were large enough to scatter blue light (ca. 400 nm), whereas the xerogels gels appear more transparent.

Quantitative Imaging. The gray value profiles $\tilde{g}_{i,\,k}$ were corrected for the anode heel effect[36] with the procedure described in SI3, resulting in the corrected gray value profiles $g_{i,\,k}$. A unique gray value of the gel at a given drying stage was calculated by averaging $g_{i,\,k}$ along the slice number i with eq 1

$$G_k = \frac{1}{\tilde{V}_k} \sum_{i=0}^{N} g_{i,k} \cdot A_{i,k} \tag{1}$$

where G_k is called the "global gray value" and N is the total number of slices. The conversion between the gray value of a voxel and the reconstructed attenuation coefficient (RAC) of the scanned material at that voxel was given by

$$g = \frac{\mu - a}{b - a} \cdot 255 \tag{2}$$

where g is a gray value in 8-bit, μ is the RAC, and a and b are, respectively, the minimum and maximum attenuation values within the volume and are called contrast parameters. In all measured samples, a and b were set at -0.90185 and 1.14111, respectively. These values were chosen so that the gray values corresponding to the voxels belonging to the sample were binned between 0 and 255 in the reconstructed images at any point of drying. The global RAC of the gel during drying $\bar{\mu}_k$ was calculated with eq 2 from the global gray values G_k. $\bar{\mu}_k$ can be expressed as the sum of the RAC of each individual phase composing the gel, weighted by their respective volume fractions

$$\bar{\mu}_k = \frac{\mu_{hex} V_{hex,k} + \mu_{skel} V_{skel}}{V_k} \tag{3}$$

where μ_{hex} and μ_{skel} are the RACs of n-hexane and of the silica skeleton and $V_{hex,\,k}$ and V_{skel} are the corresponding volumes, respectively. In eq 3, the contribution of gas phases to the global RAC, notably hexane vapor, was neglected. The contribution of hexane vapor to X-ray absorption was considered negligible compared to the one of liquid hexane. The RACs of the silica skeleton μ_{skel} and of hexane μ_{hex} as well as the skeleton volume V_{skel} were assumed to remain constant during drying. The global gray value of hexane G_{hex} was computed from the μCT scans done on a reference n-hexane sample. μ_{hex} was then calculated using eq 2 with G_{hex} averaged over the 134 last scans. At any time, the gel volume V_k reads

$$V_k = V_{hex,k} + V_{skel} + V_{air,k} \tag{4}$$

with $V_{air,\,k}$ as the volume of air or gas in the gel. At the end of drying for $k \geq k_d$, the hexane content was assumed to be zero and eq 3 becomes

$$\bar{\mu}_{k \geq k_d} = \frac{\mu_{skel} V_{skel}}{V_{k \geq k_d}} \tag{5}$$

In practice, the product $\mu_{skel} V_{skel}$ was computed by taking the average of the product between the global RAC and the volume of the gel

$$\mu_{skel} V_{skel} = \frac{1}{M} \sum_{k \geq k_d} \bar{\mu}_k V_k \tag{6}$$

where M is the number of scans between the scan k_d and the final scan. The hexane volume was calculated by substituting eq 6 in eq 3. At the beginning of the drying for $k \leq k_2$, the air content was assumed to be zero and with the knowledge of V_{hex}, the skeleton volume can be calculated with eq 7

$$V_{skel} = \frac{1}{N} \sum_{k_1 \leq k \leq k_2} V_k - V_{hex,k} \tag{7}$$

where N is the number of scans between scans k_1 and k_2. k_1 corresponds to the scan number from which the X-ray tube was assumed stable. k_d, k_1, and k_2 were chosen manually and may be different for each sample (Table S1). The air volume was directly

given in eq 4 since $V_{hex, k}$ and V_{skel} are known. Equations 3, 4, 6, and 7 form a four-equation invertible system with four unknowns: $V_{hex,k}$, $V_{air,k}$, V_{skel}, and μ_{skel}. The error propagation was calculated numerically and is documented in SI4. The error bands of all graphs correspond to the 95th percentile. The skeletal density of the gels was calculated with $\rho_{skel} = m^d/V_{skel}$.

Numerical simulations were carried out by considering a modified drying model allowing μ_{skel} and V_{skel} to vary over time and the creation of water with the term V_{H_2O}. The global gray value of water G_{H_2O} was computed from the μCT scans done on a reference deionized water sample, and μ_{H_2O} was calculated using eq 2 with G_{H_2O} averaged over the nine last scans. The details on the modified model, the assumptions, and the solving of the equations for the simulations are reported in SI5.

■ RESULTS AND DISCUSSION

Synthesis. In the surface modification process, the reaction between a silanol group and TMCS resulted in a trimethylsilyl group via reaction 8

$$\equiv Si—OH + (CH_3)_3SiCl \rightarrow \equiv Si—O—Si(CH_3)_3 + HCl \tag{8}$$
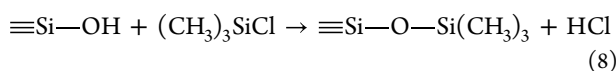
A sufficient surface modification was necessary to prevent condensation of the silanol groups and promote the spring-back effect.[37] The surface coverage of the trimethylsilyl and silanol groups was evaluated qualitatively by FTIR on a modified and unmodified gel after APD, and the spectra are shown in Figure 2. The broad peak at 1050 cm^{-1} was
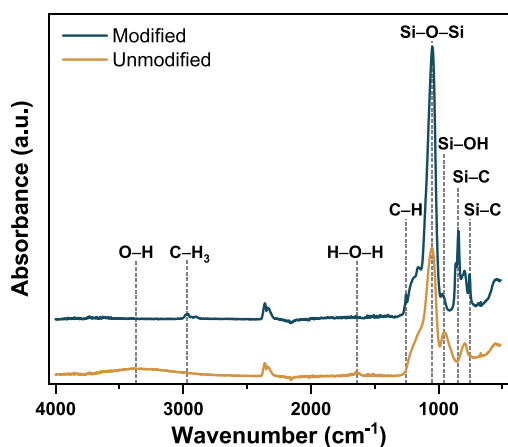

Figure 2. FTIR spectra of a modified and unmodified gel. Relevant vibration frequencies are indicated by a dashed line.

characteristic of Si—O—Si vibrations and was present in both types of gels.[38] The band at 3370 cm^{-1} and the peak at ~960 cm^{-1} originated from O—H and SiO—H vibrations, which were significant in the unmodified gel.[39] The absence of the O—H vibration band in the modified gel along with the presence of the peaks at ~2970 (C—H$_3$), 1255 (C—H), 845 (Si—C), and 756 (Si—C) cm^{-1} indicated a successful silylation of the silica skeleton.[24,38] H—O—H vibrations can be seen in the unmodified gel at ~1640 cm^{-1}, which was expected due to the hydrophilic nature of silanol groups. These results confirmed the presence of silicon—carbon and methyl bonds in the gels modified with TMCS, which was attributed to trimethylsilyl groups.

μCT Acquisition, Reconstruction, and Segmentation. Before presenting the details of the results, we present in this section the accuracy of the workflow related to the μCT data

acquisition and processing. The combination of voltage, current, and framerate of the μCT scans produced well-contrasted projections (Figure 3 and Figure S10a) leading to
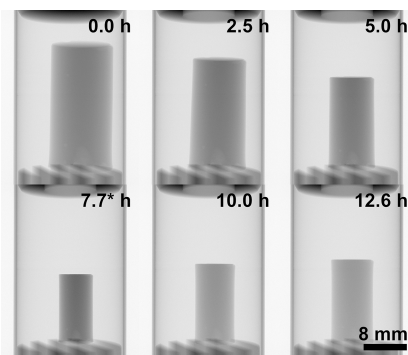

Figure 3. μCT projections of the modified gel (M4) at six stages of drying. The drying time is indicated on the top right of each projection, and the maximum shrinkage is highlighted by an asterisk.

reasonable signal-to-noise ratio and spatial resolution in the reconstructed slices (11 μm voxel^{-1}), allowing to resolve details of 40−50 μm. The drying of the gels could be accurately monitored with a 6 min time step between each scan and allowed to capture accurately the maximum shrinkage (Figure 3). Some of the μCT scans lasted longer than 1 min due to instrument errors, resulting in a lower temporal resolution especially for M1 (Figure S11). The temperature in the μCT chamber slightly increased throughout the duration of the experiment but remained within 23−25 °C (Figure S12). The low number of projections used for the reconstruction with the cone-beam algorithm introduced under-sampling artifacts in the slices.[40] This generated line patterns in the reconstructed slices (Moire patterns), which were easily visible around the sample in the background (Figure S10b). These artifacts had a negligible impact on the segmentation procedure except at the bottom of the gel close to the chamber. The ROIs obtained by automated segmentation were representative of the gel geometry (Figure S13) and were comparable to the ROIs obtained by manual segmentations independently of the sample and of the drying stage of the gel. Because of undersampling, the gray values of the voxels belonging to the sample were broadly distributed (Figure S10c). Resolving local changes in the structure was excluded given that the size of the details that can be resolved in the μCT scans was much larger than the typical size of the structure of silica aerogels (40−50 μm vs 100 nm).[32] No cracks nor pores were noticed in the μCT reconstructions of the dry gels. However, cracks smaller than 40−50 μm cannot be excluded and the under-sampling artifacts may also prevent to resolve larger cracks. Some gels moved in the chamber during drying, but the impact on the volume V_k and gray values $g_{i, k}$ computed after segmentation was negligible.

Geometric Characterization. The geometric parameters of the gels during drying were computed based on the results from the automated segmentation procedure. Figure 4 shows the volume, height, and diameter profiles versus time of a modified and unmodified gel during drying (see Figure S14 for the profiles of all seven gels). While the volume was given directly from the segmentation, the height h_k and the diameter D_k of the gel were calculated from the cross-sectional area of the gel along the z axis of the cylinder: $A_{i, k}$.
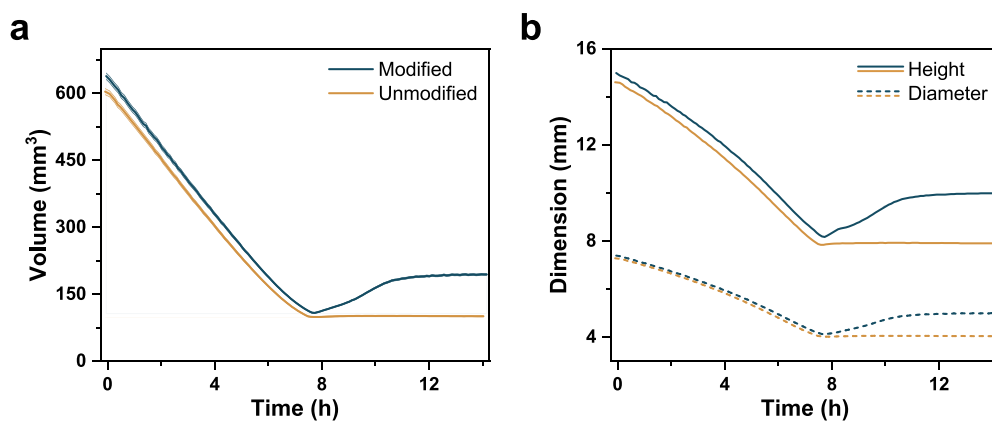
Figure 4. (a) Volume of a modified gel: M4 and an unmodified gel: U2 during ambient pressure drying. (b) Height (full line) and diameter (dashed line) of the same gels. The error bands of the height and diameter profiles are not shown. Each curve consists of 141 data points.
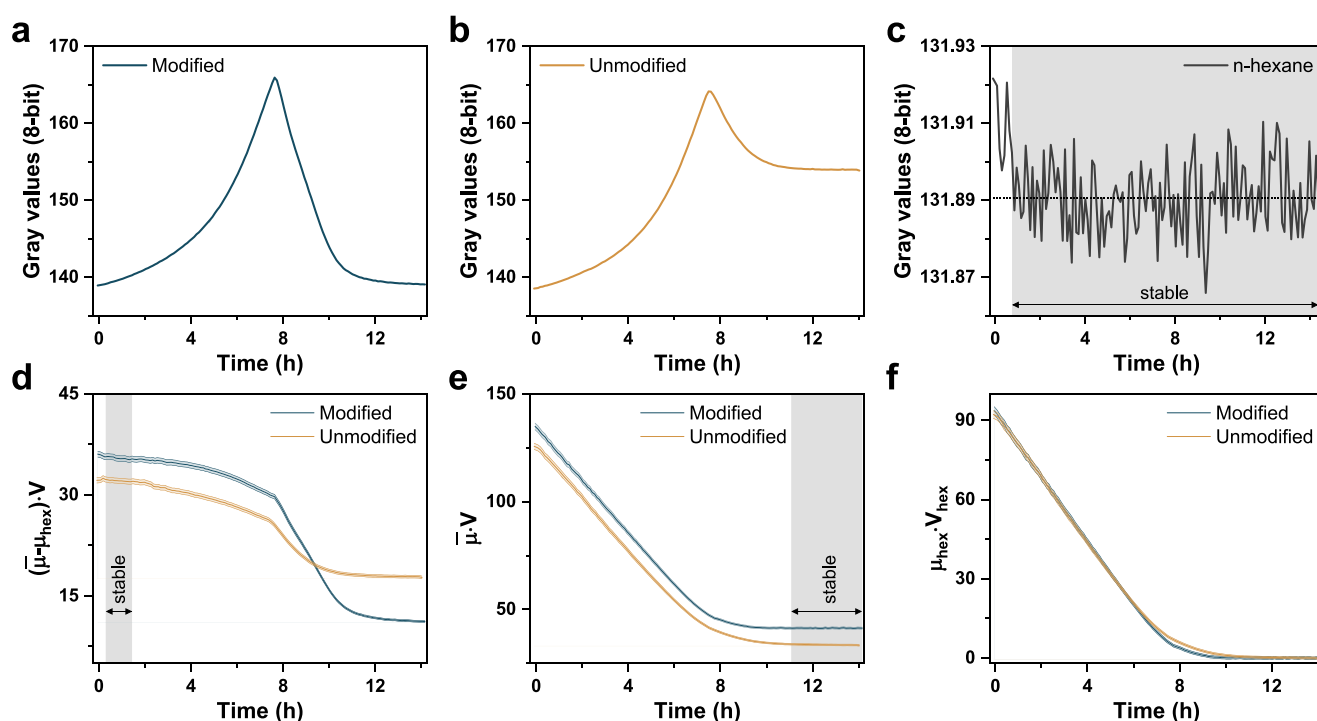

Figure 5. Intermediate data from the μCT quantitative imaging procedure. (a, b) Global gray values of a modified gel: M4 and an unmodified gel: U2 during drying. The error of the global gray values is 0.018. (c) Global gray value of an n-hexane reference sample. (d) $(\overline{\mu} - \mu_{\text{hex}}) \cdot V$ profiles of the two gels. (e) $\overline{\mu} \cdot V$ profiles. (f) $\mu_{\text{hex}} \cdot V_{\text{hex}}$ profiles. The stable region of the profiles in panels (c–e) is highlighted in gray only as indicative values. Each curve consists of 141 data points.

At the beginning of the drying, the volume was slightly different between the seven produced alcogels (Figure S14). However, the overall evolution was remarkably similar in both kinds of gels, suggesting a good reproducibility of the synthesis and drying process. For all gels, the aspect ratio h/D was rather stable throughout drying at around 2.0 (Figure S15). The initial volume of the alcogels was on average 20% smaller than the volume of the molds (785 μL). This difference was attributed to syneresis.[16,41] All samples reached the maximum shrinkage after 7−8 h of drying, and those with a higher initial volume took longer to dry. The maximum shrinkages, defined as V^{min}/V^0, were about 16.6 and 15.9 vol % for the five modified and two unmodified gels, respectively. A small difference in the maximum shrinkage of modified and unmodified gels was already reported by Smith et al. in a

similar material.[23] That difference was attributed to a real feature rather than a measurement error given the time and spatial resolution of the μCT measurements and could be due to different volumes of the silica skeleton and/or different repulsive forces within the silica network between the two types of gels. The SBE in the modified gel can be seen in Figure 4 at t = 7.7 h in the volume and height/diameter profiles and in Video S1. The spring-back efficiency was very similar between the five modified gels and was on average 29.4 vol %. Surprisingly, the two unmodified gels slightly re-expanded and recovered about 0.3% of their original volume within 2 h following the maximum shrinkage followed by a shrinkage of 0.2 vol %. Although the amount of reversible shrinkage was negligible, this confirmed that unmodified gels can relax drying-related stresses to some extent. The apparent
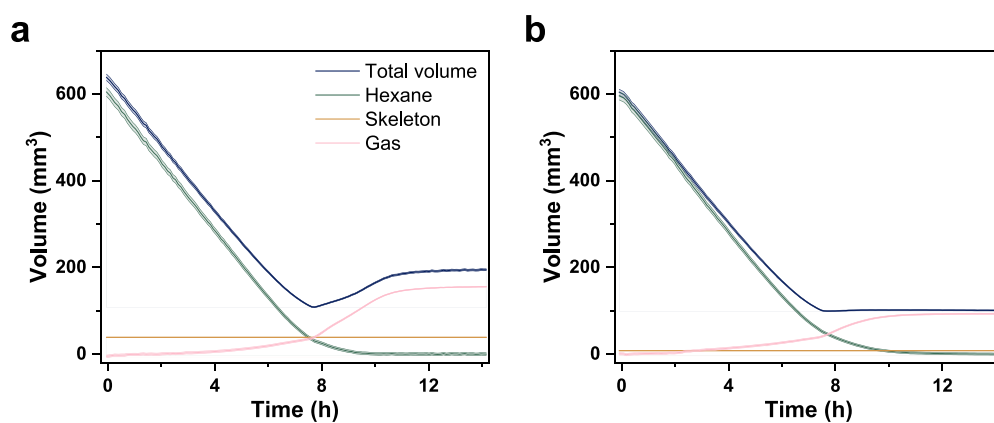
Figure 6. Total volume along with hexane, skeleton, and gas volumes of (a) a modified gel: M4 and (b) an unmodified gel: U2 during drying. Each curve consists of 141 data points.

density of the modified gels was on average 0.391 g cm^{-3}, and it was very reproducible within the five samples. The lowest and largest densities recorded were 0.384 and 0.397 g cm^{-3}, respectively. As a consequence of the limited spring-back efficiency, the produced aerogels were denser than those reported in the literature for similar synthesis and drying conditions.[14,24] This effect can arise from one or more of the following: condensation reactions (chemical lock), plastic deformation, entanglement of the solid network, and residual liquid phase (mechanical locks). It is notably possible that differences in the TMCS/SiO$_2$ molar ratio affected the capability of the gels to spring-back.[17] To this regard and complementary to FTIR, quantitative evaluation by thermogravimetric analysis (TGA) could reveal whether the extent of trimethylsilyl groups was similar compared to aerogels produced with similar synthesis conditions.[18] The two unmodified gels showed higher discrepancies with apparent densities of 0.708 and 0.648 g cm^{-3}. In fact, a variation of room humidity in combination with the hydrophilic character of unmodified gels would result in a different water intake for the two gels at the time the μCT scans were measured and until the gels were weighted. Additional μCT scans performed after a few days of further drying did not show a significant difference of the volume for both modified and unmodified gels, suggesting no residual liquid phase in the samples. The SBE was heterogeneous; on the μCT projections, it was observed that the expansion began from the top of the gel and continued downward over roughly 30 min (Video S1). Further analysis of the spatial evolution of the SBE would require a local analysis of the μCT data, a procedure not conducted in this work. To further understand the emergence of the SBE, the solid, liquid, and gas volumes during the drying of the gels were calculated using μCT quantitative imaging.

Quantitative Imaging Results. In this section, the quantitative imaging procedure and intermediate results are reported and its necessary assumptions are discussed. The μCT experiments generated two time-dependent parameters, the volume of the gel V_k and the global gray value G_k; the latter was converted into the global reconstructed attenuation coefficient $\bar{\mu}_k$ using eq 2. To calculate the volumes of the silica skeleton, hexane, and gas in the gels, the following assumptions were made: (i) at the beginning of drying, the gel consists only of the silica skeleton and hexane; (ii) at the end of drying, the gel consists only of the silica skeleton and a gas phase; (iii and iv) the hexane and silica skeleton RACs were

constant during drying; (v) the skeleton volume was constant during drying. As previously mentioned, the combination of the equations and constraints allowed us to generate an invertible system with a unique solution for the parameters of interest. The intermediate data produced by the quantitative imaging procedure are shown in Figure 5 for one modified and unmodified gel (see Figure S16 for the data on all seven gels). The global gray values were reported instead of the RACs since these are the quantities generated by the μCT reconstruction. Figure 5a,b shows the global gray values of a modified and unmodified gel. During drying, the gray values increased and reached a maximum at 7−8 h (Figure 5a,b and Figure S16a) and this time corresponded exactly to the point of maximum shrinkage in both kinds of gels (Figure 4 and Figure S14). After the maximum shrinkage, the gray value decreased and stabilized. Since the volume of the unmodified gels did not change significantly after the maximum shrinkage, the decrease in the gray value was only related to the replacement of liquid hexane for a gaseous phase. In the modified gels, the decrease in gray values originated from both the evaporation of hexane and the re-expansion of the volume. Figure 5c shows the gray values of a reference hexane sample from which an average gray value of 131.9 was calculated, equivalent to an RAC of 0.155. Instabilities of the X-ray tube were observed at the beginning of every in operando μCT experiment. As a result, slightly higher gray values were observed in the reconstructed slices for the first few μCT scans, which is notably visible in the reference hexane sample.

The skeleton volume was calculated as the average of the difference between the total volume and the hexane volume at the beginning of the drying between the lower and upper thresholds k_1 and k_2, as shown in eq 7. These thresholds allowed us to exclude the effect of the beam instabilities at the beginning of the experiment and also to provide better statistics. k_1 and k_2 were set by analyzing the quantity ($\bar{\mu}_k - \mu_{\text{hex}})V_k$, which could be seen as a mass conservation equation. Besides hexane evaporation, a gel could be considered as a closed system as long as there is no gaseous phase present. This assumption permits to write the conservation of the quantity

$$[\bar{\mu} V - \mu_{\text{hex}} V_{\text{hex}}]_{k_1 \le k \le k_2} = \text{constant} \tag{9}$$

Combining eq 9 with eq 4 and recalling the assumption that μ_{skel} and V_{skel} are set as constants and that the volume of gas is $V_{\text{air}, k_1 \le k \le k_2} = 0$ during drying lead to

$$[(\overline{\mu} - \mu_{hex})V]_{k_1 \le k \le k_2} = \text{constant} \qquad (10)$$

The quantity $(\overline{\mu}_k - \mu_{hex})V_k$ is shown in Figure 5d for a modified and unmodified gel and in Figure S16b for all gels. The plateau region where eq 10 was stable at the beginning of the drying was different between the samples, ranging from 6 to 120 min ($k_2 - k_1$ in Table S1). A plateau region at the end of the drying was also defined for the calculation of the product $\mu_{skel}V_{skel}$ calculated in eq 6 at $k \ge k_d$. k_d was determined from the $\overline{\mu}_k V_k$ profiles and was set at about 13.7 h (Figure 5e and Figure S16c and Table S1). Figure 5f and Figure S16d also show the quantity $[\mu_{hex}V_{hex}]_k$ before the division by the RAC of hexane calculated from the hexane reference sample. From these intermediate results, the remaining parameters needed to solve the system of four equations were determined, allowing the evaluation of the amount of silica skeleton, hexane, and gas of the gels during drying.

Phase Composition during Drying. The quantitative imaging procedure coupled with the underlying model of drying silica gels was used to calculate their phase composition throughout APD. Figure 6 shows the time-dependent volume profiles of the skeleton, hexane, and gas in a modified gel and unmodified gel (see Figure S17 for the other gels). The results for the five modified gels were compiled in a ternary plot showing the volume fraction of each phase (Figure 7). The
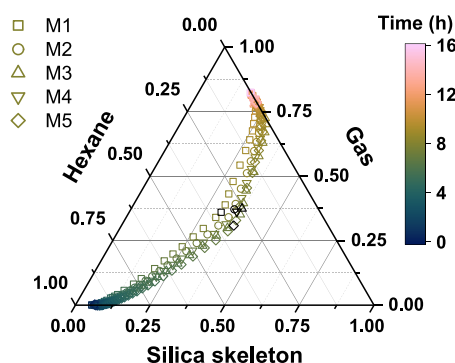

Figure 7. Ternary plot of the volume fraction of hexane, skeleton, and gas in the five modified gels during drying. The drying stage of the gel is indicated on each symbol with a color scale. The maximum shrinkage is highlighted by black symbols at the center of the graph. Only half of the data points are represented to enhance readability (71 in total).

phase composition analysis seemed to provide reproducible results between the different modified gels with the exception of M1, which seemed to be off-trend. At the beginning of drying, the porosity of all modified gels was about 95%. In some gels, the calculated air volume was negative over the first few scans due to beam instabilities and it should not be considered as a physical feature. The steady decrease in the hexane profile showed that the evaporation rate was constant for the first 6 h (Figure 6 and Figure S17), suggesting that the slight increase in temperature in the instrument had no impact on the drying dynamic as the temperature stabilized at 4−6 h (Figure S12). The hexane profiles were similar between modified and unmodified gels. In parallel to the evaporation, there was a decrease in the gel surface area where the mass transfer occurs (in Figure 4 and Figure S14 from the height and diameter profiles assuming a perfect cylinder). Therefore, the evaporation rate per surface area increased until the maximum shrinkage as already reported elsewhere,[23] which

implied that the mass transfer at the outer surface of the gel was not the limiting factor in the drying rate. This suggested that the drying rate was only limited by the convection of hexane vapor within the drying chamber for the first 6 h. A previous study reported an increasing evaporation rate in similar gels, which may be related to a difference in the ambient conditions compared to this study.[24] Interestingly, we calculated a significant amount of gas phase in all gels already before the maximum shrinkage, making for up to 37 vol % of the gel's volume (Figures 6 and 7 and Figure S17). This suggested that the liquid−gas interface already receded into the pores, whereas common drying models predict that the liquid recedes in the pores once shrinkage stops.[42] This finding was supported by the small decrease in the hexane evaporation rate before maximum shrinkage (Figure 6 and Figure S17), indicating that the transport of hexane vapor became limited by its diffusion through the pore network rather than by the convection within the drying chamber. It is worth noting that upon visual inspection of modified gels dried ex situ in glass containers, they remained transparent until the maximum shrinkage and only turned opaque afterward. Although the drying conditions were different compared to the μCT drying chamber, we can reasonably assume that the gels underwent similar changes in the in operando μCT experiments. This could mean that the volume occupied by gas/air in the pores was too small to scatter light prior to the SBE.[42]

The emergence of the SBE could be related to a particular state of the gel, composed of nearly equal volume fractions of silica skeleton, hexane, and gas phases (Figures 6 and 7 and Figure S17). This composition arguably corresponds to a critical drying stage where some pores get completely depleted in hexane. Consequently, the silica skeleton was able to relax the drying-related stresses, generating a spring-back visible on a macroscopic level. Such critical composition would depend on the morphology and structure of the silica network and thus on the synthesis conditions. Given that the quantitative imaging approach only provided the average volume of hexane and gas, it could not be ruled out that this critical composition was a consequence of heterogeneous phase composition in the gels, e.g., that the top part of the gel dried faster than the bottom part. To exclude heterogeneities would require investigating the local phase composition of the gels during drying. However, μCT projections revealed a homogeneous evolution of the diameter and height (Video S1) prior to the SBE, suggesting a homogeneous phase composition. Moreover, the gray value profiles along the vertical axis of the gel only changed significantly after the SBE (Figure S5). The SBE seemed to happen in two regimes: at first, the volume expansion rate was rather steady, and after about 80 min, it slightly increased. The moment of increasing rate corresponded to the point where the fraction of hexane went below ~5 vol % of the pore volume for all modified gels (Figure 6a and Figure S17). Nevertheless, the analysis of the average phase composition of the gels after spring-back was limited due to the slightly heterogeneous SBE (Video S1). The abrupt change of hexane and gas volume profiles at the maximum shrinkage may be an artifact related to the correction of the anode heel effect as it was difficult to fit the gray value profiles during the SBE (SI3). In the unmodified gels, the shrinkage stopped once the hexane and gas volumes were roughly equal followed by a decreasing evaporation rate (Figure 6b and Figure S17e).
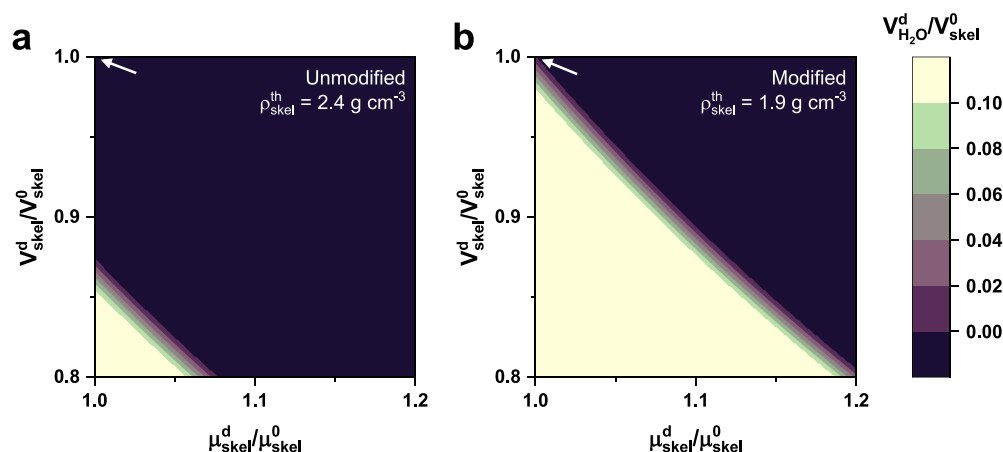
Figure 8. Maps resulting from numerical simulations implementing condensation reactions during the drying of (a) an unmodified gel: U2 and (b) a modified gel: M4 assuming theoretical skeleton densities of 2.4 and 1.9 g cm^{-3} for the unmodified and modified gel, respectively. The x axis corresponds to the relative change in the skeleton RAC between the end and the beginning of the drying. The y axis corresponds to the relative change in the skeleton volume. The colored scale bar shows the relative volume of water in the gel at the end of the drying. Each trio of values located on the contour surfaces within $0 \leq V^d_{H_2O}/V^0_{skel} \leq 0.1$ satisfies $\rho_{skel} = \rho^0_{skel}$. Points located outside of this range are not shown. The arrows highlight the theoretical point corresponding to no condensation reactions. The maps resolution is 100×100 data points.

The skeleton volume of the modified gel shown in Figure 6 was about 39 mm^3 and varied from 33 to 38 mm^3 in the other gels (Figure S17). The average skeletal density for the five modified gels was 1.97 ± 0.14 g cm^{-3}, showing consistent reproducibility between the five samples. The calculated densities were in the range of typical values for silica aerogels reported in the literature by helium pycnometry.[20,24] These findings emphasized the reliability of the μCT quantitative imaging procedure and the accuracy of the underlying model for the modified gels. It is pertinent to be aware about the impact of potential closed pores in the calculation of the skeleton volume. Closed pores being inaccessible by helium lead to an overestimation of the skeleton volume and thus to an underestimation of the skeleton density. Using μCT, closed pores still filled with hexane at the end of drying would result in an overestimated global RAC and thus in an overestimation of the skeleton volume as well. The remaining amount of hexane in the aerogels may be quantified by comparing the weight of the gels before and after heat treatment, which can also enable further volume recovery.[16] It must also be noted that small changes in the hexane volume (and hexane RAC) had a large impact on the skeleton volume since it was calculated as the difference between two large quantities: the total volume and the hexane volume as shown in eq 7. Finally, eventual unresolved cracks in the μCT volumes appearing during drying would essentially be interpreted as "pores" in the drying model. These would result in a higher gas content but would not have consequences on the skeleton or hexane volumes since the quantity $[\bar{\mu}V]_{k \geq k_d}$ in eq 5 is independent of the gas volume.

The quantitative imaging procedure applied to unmodified gels resulted in substantially underestimated skeleton volume, which led to very different skeletal densities of the xerogels at 3.7 and 8.4 g cm^{-3}, much higher than the density of silica glass (2.2 g cm^{-3}). Given the dependency of the skeleton, hexane, and gas volumes in eq 4, the hexane and gas volume profiles of the unmodified gels reported in Figure 6b were affected by the underestimated skeleton volume and were thus erroneous. A difference between unmodified and modified gels was also observed in the raw data from the quantitative imaging

procedure. The profiles $\bar{\mu}_k V_k$ of U1 and U2 started at a similar value as M3 and M5 at the beginning of the drying but reached a lower plateau at the end of the drying (Figure S16c). That difference could not be caused by the residual amount of hexane in the unmodified gels since it would increase the RAC. We propose that the abnormal quantities calculated for the unmodified gels were due to limitations in the modeling of the phase composition evolution. More specifically, the assumption of a constant skeleton RAC and volume may not be valid in the unmodified gels due to condensation reactions occurring during the drying shrinkage. To complement the phase composition analysis, we performed simulations based on the quantitative imaging results including potential condensation reactions between surface silanol groups in the model.

Condensation during Shrinkage. Water condensation reactions between surface silanol groups may occur during the APD of silica gels, resulting in the creation of siloxane bonds, which leads to irreversible shrinkage of the silica network[43]

$$\equiv Si-OH + HO-Si\equiv \rightarrow \equiv Si-O-Si\equiv + H_2O \tag{11}$$
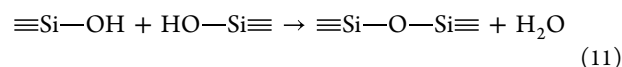
The assumptions of the model were modified to include in the equations a change in skeleton volume and RAC as well as a term corresponding to the created water. For simplicity, the simulations were not performed over time but only comparing the state of a gel at the beginning and at the end of drying. The derivation of the modified model and corresponding solution of the simulations are reported in SI5. By taking into account the condensation reactions, the number of unknowns in the four-equation system increased from four to seven. The skeletal density was fixed and set at 1.9 g cm^{-3} for the modified gels and at 2.4 g cm^{-3} for the xerogels.[24] Despite the additional constraint, the resulting system had two more unknowns than equations and the simulations generated an infinite number of solutions as 2D surfaces. We chose to evaluate the change of the following quantities: $C_V = V^d_{skel}/V^0_{skel}$, $C_\mu = \mu^d_{skel}/\mu^0_{skel}$, and $C_H = V^d_{H_2O}/V^d_{skel}$. C_V and C_μ represent the relative change of the skeleton volume and RAC between the dry gel (superscript d) and the alcogel (superscript 0), respectively. C_H represents the intake of water in the dry gel relative to the final skeleton

Table 1. Main Properties of the Five Modified and Two Unmodified Gels Dried at Ambient Pressure[a]

sample	volume change upon gelation or syneresis (vol %)	maximum shrinkage (vol %)	time of maximum shrinkage (h)	spring-back efficiency (vol %)	porosity of the alcogel (vol %)	porosity of the dry gel (vol %)	apparent density (g cm^{-3})	dry skeletal density (g cm^{-3})
M1	14.8	16.2	8.1	28.5	95.9	82.4	0.394	2.251
M2	17.0	16.4	8.0	29.1	95.4	80.1	0.397	2.025
M3	22.8	16.5	7.4	29.0	94.8	80.0	0.391	1.853
M4	18.6	16.9	7.7	30.5	94.7	80.0	0.384	1.922
M5	24.4	16.9	7.1	29.8	93.4	78.7	0.387	1.820
U1	21.9	15.5	7.8	15.5	97.4*	81.4*	0.708	3.741*
U2	23.0	16.4	7.8	16.7	98.6*	93.0*	0.648	8.443*

[a]The values with a (*) superscript were calculated from the underestimated skeleton volume in the unmodified gels and are thus not representative.

volume V_{skel}^{d}. For the sake of visualization, we assumed that the change in skeleton volume and RAC would not exceed 20% and that the final water intake would not be larger than 10% of the dry skeleton volume. Therefore, the simulations were performed for $0.8 \leq C_V \leq 1.0$, $1.0 \leq C_\mu \leq 1.2$, and $0 \leq C_H \leq 0.1$. The results from the simulations are shown in Figure 8 for an unmodified and modified gel, and simulations on the other gels are shown in Figure S18. The domain over which $0 \leq C_H \leq 0.1$ was valid corresponds to the slightly curved band in Figure 8. In the unmodified gel, the band was considerably distant from the point $(C_V, C_\mu, C_H) = (1,1,0)$, which corresponded to a model excluding condensation reactions. Simulations suggested that a skeleton volume shrinkage of at least 13 vol % of its original value, corresponding to $C_V = 0.87$, would be necessary for reaching a target density of 2.4 g cm^{-3} for the dry silica skeleton in unmodified gels. Although all points on the curved surface were theoretically valid in the simulation framework, only part of them was physically relevant, e.g., a decrease in skeleton volume without water intake would not be a physical feature.

In the modified gels, the point of no condensation reactions was included in the curved surface with $0 \leq C_H \leq 0.1$ (Figure 8b). Therefore, a target dry skeletal density of 1.9 g cm^{-3} could theoretically be possible without any condensation reactions. This emphasizes the successful modification by TMCS. These results also support the fact that the relatively low spring-back efficiency was not due to a chemical lock of the silica network by condensation reactions but possibly by mechanical locking of the silica network. The simulations on the condensation reactions based on the quantitative imaging analysis showed that the change of skeleton volume was potentially significant during APD of unmodified gels, while it was potentially negligible in the modified gels. Table 1 summarizes the key quantities computed by μCT segmentation and quantitative imaging for all gels.

CONCLUSIONS

This study addressed the phase composition evolution of silylated silica aerogels during ambient pressure drying by an in operando μCT approach. The quantitative imaging workflow was more reliable to characterize modified gels than unmodified gels, which was attributed to the drying-related condensation reactions occurring in the latter.

The emergence of the spring-back effect in the silylated gels coincided with volume fractions of the skeleton, hexane, and gas reaching roughly one-third each during drying. We proposed that at this threshold composition, some pores got locally depleted in hexane, which enabled the relaxation of the capillary stresses by the silica skeleton, thus enabling the SBE.

At first, the re-expansion was slow due to significant amounts of hexane remaining in the pores. Once the hexane went below roughly 5 vol % of the total pore volume, the expansion rate increased slightly as more of the silica skeleton was able to relax. The expansion stabilized, and the gels volume plateaued at 29 vol % of their initial volume, resulting in monolithic aerogels. The results suggest that this relatively low spring-back efficiency could be attributed to an irreversible plastic deformation and/or remaining stress in the solid network. We anticipate that further expansion was mostly hindered by the entanglement of the silica network and that the structure could be unlocked by overcoming some activation energy. Further analysis of the data collected by μCT would provide more insights on the dynamic of the SBE in silica aerogels, in particular by evaluating the local phase composition of drying gels rather than the overall phase composition. We also emphasize the potential of lab-source CT instruments as a tool for materials scientists to perform phase compositional analysis of materials undergoing geometric and compositional transformations over time.

ASSOCIATED CONTENT

Supporting Information

The Supporting Information is available free of charge at https://pubs.acs.org/doi/10.1021/acs.chemmater.3c01451.

Animation of 141 μCT projections during the ambient pressure drying of a modified gel (MP4)

PEEK mold and drying chamber photographs, details on the automated segmentation script, procedure for the correction of the gel's volume and the anode heel effect, error propagation calculation, equation system for the condensation reaction simulation, gray values in a reconstructed slice, timestamp and temperature of in operando μCT scans, 3D volume resulting from the segmentation, volume, aspect ratio, diameter, and height profiles along with the phase composition profiles and simulation maps of the other modified/unmodified gels, and secondary parameters for the quantitative imaging procedure (PDF)

AUTHOR INFORMATION

Corresponding Authors

Julien Gonthier − Department of Biomaterials, Max Planck Institute of Colloids and Interfaces, 14476 Potsdam, Germany; orcid.org/0000-0001-5257-4688; Email: julien.gonthier@mpikg.mpg.de

Peter Fratzl − Department of Biomaterials, Max Planck Institute of Colloids and Interfaces, 14476 Potsdam,

Germany;   ⊙ orcid.org/0000-0003-4437-7830;
Email: fratzl@mpikg.mpg.de

Wolfgang Wagermaier − *Department of Biomaterials, Max
Planck Institute of Colloids and Interfaces, 14476 Potsdam,
Germany*; Email: wolfgang.wagermaier@mpikg.mpg.de

Authors

Tilman Rilling − *Department of Biomaterials, Max Planck
Institute of Colloids and Interfaces, 14476 Potsdam,
Germany*

Ernesto Scoppola − *Department of Biomaterials, Max Planck
Institute of Colloids and Interfaces, 14476 Potsdam,
Germany*; ⊙ orcid.org/0000-0002-6390-052X

Fabian Zemke − *Chair of Advanced Ceramic Materials,
Institute of Materials Science and Technology, Faculty III
Process Sciences, Technische Universität Berlin, 10623 Berlin,
Germany*

Aleksander Gurlo − *Chair of Advanced Ceramic Materials,
Institute of Materials Science and Technology, Faculty III
Process Sciences, Technische Universität Berlin, 10623 Berlin,
Germany*; ⊙ orcid.org/0000-0001-7047-666X

Complete contact information is available at:
https://pubs.acs.org/10.1021/acs.chemmater.3c01451

Author Contributions

Conceptualization and methodology: J.G., P.F., and W.W.;
design of the experimental setup: J.G., F.Z., and W.W.;
software: J.G. and E.S.; formal analysis: J.G.; investigation and
data curation: J.G. and T.R.; writing−original draft and
visualization: J.G. and W.W.; writing−review and editing:
J.G., T.R., E.S., F.Z., A.G., P.F., and W.W.; supervision: P.F.
and W.W.; project administration: J.G., W.W., and P.F.;
funding acquisition: A.G. and W.W.

Notes

The authors declare no competing financial interest.

■ REFERENCES

(1) Hüsing, N.; Schubert, U. Aerogels - Airy Materials: Chemistry,
Structure, and Properties. *Angew. Chem. Int. Ed.* **1998**, *37*, 22−45.

(2) Vareda, J. P.; Lamy-Mendes, A.; Durães, L. A reconsideration on
the definition of the term aerogel based on current drying trends.
Microporous Mesoporous Mater. **2018**, *258*, 211−216.

(3) Baetens, R.; Jelle, B. P.; Gustavsen, A. Aerogel insulation for
building applications: A state-of-the-art review. *Energy Build.* **2011**, *43*,
761−769.

(4) Kanamori, K.; Ueoka, R.; Kakegawa, T.; Shimizu, T.; Nakanishi,
K. Hybrid silicone aerogels toward unusual flexibility, functionality,
and extended applications. *J. Sol-Gel Sci. Technol.* **2019**, *89*, 166−175.

(5) Liu, W.; et al. Noble Metal Aerogels—Synthesis, Character-
ization, and Application as Electrocatalysts. *Acc. Chem. Res. Feb.* **2015**,
48, 154−162.

(6) Venkateswara Rao, A.; Hegde, N. D.; Hirashima, H. Absorption
and desorption of organic liquids in elastic superhydrophobic silica
aerogels. *J. Colloid Interface Sci.* **2007**, *305*, 124−132.

(7) Smirnova, I.; Gurikov, P. Aerogels in chemical engineering:
Strategies toward tailor-made aerogels. *Annu. Rev. Chem. Biomol. Eng.*
2017, *8*, 307−334.

(8) Soleimani Dorcheh, A.; Abbasi, M. H. Silica aerogel; synthesis,
properties and characterization. *J. Mater. Process. Technol.* **2008**, *199*,
10−26.

(9) Wernery, J.; Mancebo, F.; Malfait, W. J.; O'Connor, M.; Jelle, B.
P. The economics of thermal superinsulation in buildings. *Energy
Build.* **2021**, *253*, No. 111506.

(10) Carroll, M. K.; Anderson, A. M.; Mangu, S. T.; Hajjaj, Z.;
Capron, M. Aesthetic Aerogel Window Design for Sustainable
Buildings. *Sustainability* **2022**, *14*, 2887.

(11) Ganobjak, M.; Malfait, W. J.; Just, J.; Käppeli, M.; Mancebo, F.;
Brunner, S.; Wernery, J. Get the light & keep the warmth - A highly
insulating, translucent aerogel glass brick for building envelopes. *J.
Build. Eng.* **2023**, *64*, No. 105600.

(12) Shi, F.; Wang, L.; Liu, J. Synthesis and characterization of silica
aerogels by a novel fast ambient pressure drying process. *Mater. Lett.*
2006, *60*, 3718−3722.

(13) Prakash, S. S.; Sankaran, C. J.; Hurd, A. J.; Rao, S. M. Silica
aerogel films prepared at ambient pressure by using surface
derivatization to induce reversible drying shrinkage. *Nature* **1995**,
374, 439−443.

(14) Wei, T. Y.; Chang, T. F.; Lu, S. Y.; Chang, Y. C. Preparation of
monolithic silica aerogel of low thermal conductivity by ambient
pressure drying. *J. Am. Ceram. Soc.* **2007**, *90*, 2003−2007.

(15) Xian-lang, Q.; Min, Y.; Hong, L.; Jia-wen, X.; Mu-su, R.; Jin-
liang, S. Optimized preparation of thermal insulation hydrophobic
SiO2 aerogel based on orthogonal design method. *J. Porous Mater.*
2022, *29*, 1037.

(16) Hwang, S.-W.; Jung, H.-H.; Hyun, S.-H.; Ahn, Y.-S. Effective
preparation of crack-free silica aerogels via ambient drying. *J. Sol-Gel
Sci. Technol.* **2007**, *41*, 139−146.

(17) Hwang, S.-W.; Kim, T.-Y.; Hyun, S.-H. Effect of surface
modification conditions on the synthesis of mesoporous crack-free
silica aerogel monoliths from waterglass via ambient-drying. *Micro-
porous Mesoporous Mater.* **2010**, *130*, 295−302.

(18) Zemke, F.; et al. Origin of the Springback Effect in Ambient-
Pressure-Dried Silica Aerogels: The Effect of Surface Silylation. *Gels*
2023, *9*, 160.

(19) Rao, A. P.; Rao, A. V.; Pajonk, G. M. Hydrophobic and Physical
Properties of the Two Step Processed Ambient Pressure Dried Silica
Aerogels with Various Exchanging Solvents. *J. Sol-Gel Sci. Technol.*
2005, *36*, 285−292.

(20) Rao, A. P.; Pajonk, G. M.; Rao, A. V. Effect of preparation
conditions on the physical and hydrophobic properties of two step
processed ambient pressure dried silica aerogels. *J. Mater. Sci.* **2005**,
40, 3481−3489.

(21) Bangi, U. K. H.; Venkateswara Rao, A.; Parvathy Rao, A. A new
route for preparation of sodium-silicate-based hydrophobic silica
aerogels via ambient-pressure drying. *Sci. Technol. Adv. Mater.* **2008**, *9*,
35006.

(22) Sivaraman, D.; Zhao, S.; Iswar, S.; Lattuada, M.; Malfait, W. J.
Aerogel Spring-Back Correlates with Strain Recovery: Effect of Silica
Concentration and Aging. *Adv. Eng. Mater.* **2021**, *23*, 2100376.

(23) Smith, D. M.; Stein, D.; Anderson, J. M.; Ackerman, W. Preparation of low-density xerogels at ambient pressure. *J. Non-Cryst. Solids* **1995**, *186*, 104−112.

(24) Zemke, F.; Scoppola, E.; Simon, U.; Bekheet, M. F.; Wagermaier, W.; Gurlo, A. Springback effect and structural features during the drying of silica aerogels tracked by in-situ synchrotron X-ray scattering. *Sci. Rep.* **2022**, *12*, 7537.

(25) Stojanovic, A.; Paz Comesaña, S.; Rentsch, D.; Koebel, M. M.; Malfait, W. J. Ambient pressure drying of silica aerogels after hydrophobization with mono-, di- and tri-functional silanes and mixtures thereof. *Microporous Mesoporous Mater.* **2019**, *284*, 289−295.

(26) Iswar, S.; Malfait, W. J.; Balog, S.; Winnefeld, F.; Lattuada, M.; Koebel, M. M. Effect of aging on silica aerogel properties. *Microporous Mesoporous Mater.* **Mar. 2017**, *241*, 293−302.

(27) Malfait, W. J.; et al. Surface Chemistry of Hydrophobic Silica Aerogels. *Chem. Mater.* **Oct. 2015**, *27*, 6737−6745.

(28) Kohns, R.; Torres-Rodriguez, J.; Euchler, D.; Seyffertitz, M.; Paris, O.; Reichenauer, G.; Enke, D.; Huesing, N. Drying of Hierarchically Organized Porous Silica Monoliths-Comparison of Evaporative and Supercritical Drying. *Gels* **2023**, *9*, 71.

(29) Peterlik, H.; Fratzl, P. Small-Angle X-Ray Scattering to Characterize Nanostructures in Inorganic and Hybrid Materials Chemistry. *Monatshefte für Chemie / Chem. Mon.* **2006**, *137*, 529−543.

(30) Vásárhelyi, L.; Kónya, Z.; Kukovecz, Á.; Vajtai, R. Micro-computed tomography−based characterization of advanced materials: a review. *Mater. Today Adv.* **2020**, *8*, No. 100084.

(31) Yada, N.; Onishi, H. Validation of computed tomography-based attenuation correction of deviation between theoretical and actual values for four computed tomography scanners. *Asia Ocean. J. Nucl. Med. Biol.* **2016**, *4*, 81−89.

(32) Pierre, A. C., Rigacci, A., "SiO2 Aerogels," in *Aerogels Handbook*, Aegerter, M. A., Leventis, N., Koebel, M. M., Eds. New York, NY: Springer New York, 2011, pp. 21−45.

(33) Borisenko, N. G.; Akunets, A. A.; Artyukov, I. A.; Gorodnichev, K. E.; Merkuliev, Y. A. X-Ray Tomography of Growing Silica Gel with a Density Gradient. *Fusion Sci. Technol.* **2009**, *55*, 477−483.

(34) Borisenko, N. G.; Nazarov, W.; Musgrave, C. S. A.; Merkuliev, Y. A.; Orekhov, A. S.; Borisenko, L. A. Characterization of divinyl benzene aerogels with density gradient using X-ray tomography technique. *J. Radioanal. Nucl. Chem.* **2014**, *299*, 961−964.

(35) "Dragonfly." Object Research Systems (ORS) Inc, Montreal, Canada, 2022, [Online]. Available: http://www.theobjects.com/dragonfly.

(36) Kusk, M. W.; Jensen, J. M.; Gram, E. H.; Nielsen, J.; Precht, H. Anode heel effect: Does it impact image quality in digital radiography? A systematic literature review. *Radiography* **2021**, *27*, 976−981.

(37) Bisson, A.; Rigacci, A.; Lecomte, D.; Rodier, E.; Achard, P. Drying of Silica Gels to Obtain Aerogels:Phenomenology and Basic Techniques. *Drying Technol.* **Jan. 2003**, *21*, 593−628.

(38) Al-Oweini, R.; El-Rassy, H. Synthesis and characterization by FTIR spectroscopy of silica aerogels prepared using several Si(OR)4 and R″Si(OR′)3 precursors. *J. Mol. Struct.* **2009**, *919*, 140−145.

(39) Brinker, C. J., Scherer, G. W., CHAPTER 9 - Structural Evolution during Consolidation, In *Sol-Gel Science*, Brinker, C. J., Scherer, G. W., Eds. San Diego: Academic Press, 1990, pp. 514−615, .

(40) Schulze, R.; Heil, U.; Groβ, D.; Bruellmann, D. D.; Dranisehnikow, E.; Schwanecke, U.; Schoemer, E. Artefacts in CBCT: a review. *Dentomaxillofacial Radiol.* **Jul. 2011**, *40*, 265−273.

(41) Brinker, C. J., Scherer, G. W., CHAPTER 6 - Aging of Gels, In *Sol-Gel Science*, Brinker, C. J., Scherer, G. W., Eds. San Diego: Academic Press, 1990, pp. 356−405, .

(42) Brinker, C. J., Scherer, G. W., CHAPTER 8 - Drying, In *Sol-Gel Science*, Brinker, C. J., Scherer, G. W., Eds. San Diego: Academic Press, 1990, pp. 452−513, .

(43) Brinker, C. J., Scherer, G. W., CHAPTER 3 - Hydrolysis and Condensation II: Silicates, In *Sol-Gel Science*, Brinker, C. J., Scherer, G. W., Eds. San Diego: Academic Press, 1990, pp. 96−233.

📖 Recommended by ACS